PHYSICAL REVIEW A **110**, 023711 (2024)

Phase transitions and dynamic currents in a pseudo-Hermitian system of coupled sites with tunable gain and loss

Yan-Zi Jing,[1] Ke-Wen Xiao,[2,*] and Wen-Yuan Wang[1,†]
[1]*College of Physics and Electronic Engineering, Northwest Normal University, Lanzhou 730070, China*
[2]*School of Physics and Astronomy, Rochester Institute of Technology, Rochester, New York 14623, USA*

(Received 18 April 2024; accepted 24 July 2024; published 7 August 2024)

The investigation of pseudo-Hermitian systems has garnered widespread attention due to their distinctive property of purely real eigenvalues splitting into complex conjugate pairs. This transition profoundly modifies the system's behavior, specifically giving rise to remarkable dynamical effects. Here we explore the novel characteristics of phase transitions and dynamic currents in a pseudo-Hermitian system of coupled sites with tunable gain and loss. With tunable gain and loss, we verify that the system uniquely supports two pseudo-Hermitian configurations, which exhibit distinct symmetries. The phase transitions from the $\mathcal{PT}$-symmetric phase to the spontaneous broken $\mathcal{PT}$-symmetric phase, along with the associated high-order exceptional points (EPs), are unambiguously demonstrated in both types of symmetry configurations. We measure the dynamic current within the four coupled sites, which allows us to probe the EPs and phase transitions between distinct phases. Our results offer insights into the phase transitions and dynamics of pseudo-Hermitian systems, with potential applications in the design and manipulation of novel quantum phenomena across various fields including photonics and other related quantum systems.

DOI: 10.1103/PhysRevA.110.023711

I. INTRODUCTION

In standard quantum mechanics, observables are typically characterized by Hermitian operators. For a Hermitian Hamiltonian, expressed as $H = H^\dagger$, its eigenvalues are inherently real and its temporal evolution is unitary, rendering it suitable for describing isolated systems. However, in practical scenarios, it becomes imperative to account for the influence of the surrounding environment on the system. Under certain circumstances, these environmental effects can be effectively captured using non-Hermitian Hamiltonians [1,2]. For instance, systems exhibiting gain or loss are frequently described by non-Hermitian Hamiltonians, $H \neq H^\dagger$, where probability conservation is generally violated and the temporal evolution is nonunitary [3–6].

Nevertheless, if a non-Hermitian Hamiltonian H satisfies the pseudo-Hermitian condition $H^\dagger = \eta H \eta^{-1}$ with η being a linear Hermitian operator, its eigenenergy can be either purely real or exist as complex conjugate pairs [7]. In 1998, Bender and colleagues pointed out that a non-Hermitian Hamiltonian possessing parity-time ($\mathcal{PT}$) symmetry can also exhibit a completely real energy eigenvalue spectrum. Here, $\mathcal{P}$ and $\mathcal{T}$ represent the operators of parity and time-reversal transformations, respectively, defined as $\mathcal{P}(x \to -x, p \to -p)$ and $\mathcal{T}(x \to x, p \to -p, i \to -i)$ [8,9]. The $\mathcal{PT}$-symmetric Hamiltonian, satisfying $[H, \mathcal{PT}] = 0$, constitutes a special subset of pseudo-Hermitian Hamiltonians [10]. Notably, it was later demonstrated that non-$\mathcal{PT}$ invariant systems possessing real eigenvalues are also pseudo-Hermitian [11,12].

Pseudo-Hermitian systems exhibit a range of intriguing behaviors [13,14], with a pivotal characteristic being the ability to induce a spontaneous $\mathcal{PT}$-symmetric phase transition by adjusting a parameter within the system. In the unbroken $\mathcal{PT}$ symmetry phase, the system exhibits a completely real energy eigenvalue spectrum and all eigenfunctions of the Hamiltonian simultaneously serve as eigenfunctions of the $\mathcal{PT}$ operator, signifying their $\mathcal{PT}$ symmetry. Conversely, in the spontaneous broken $\mathcal{PT}$ symmetry phase, the energy eigenvalue spectrum transforms into a partially or fully complex spectrum with conjugate-paired eigenvalues and not all eigenfunctions retain $\mathcal{PT}$ symmetry [15,16]. A phase transition occurs as the system transitions from a $\mathcal{PT}$-symmetric phase to a spontaneous broken $\mathcal{PT}$-symmetric phase. This transition is marked by the merging of two eigenvalues and their corresponding eigenvectors, corresponding to exceptional points (EPs) [16–18]. The existence of a continuous set of EPs that delineate regions with $\mathcal{PT}$-symmetric phase and spontaneous broken $\mathcal{PT}$-symmetric phase are known as exceptional lines (ELs) [19]. Furthermore, the higher-order EPs have been previously reported in pseudo-Hermitian cavity optomechanical system [20,21] and cavity-magnon system [22]. In recent years, pseudo-Hermitian systems have been realized in various experimental setups, such as lasers [23–25], waveguides [26–30], microwave cavities [31,32], and optical resonators [33,34], trapped ion [35,36], and hybrid quantum system [37], to name a few.

The dynamics exhibited by pseudo-Hermitian systems are distinctly characterized by the occurrence of phase transitions, providing a deeper understanding of these systems [38,39].

---

[*] Contact author: kewenxiao@gmail.com

[†] Contact author: wywang@nwnu.edu.cn

Notably, while the investigation of $\mathcal{PT}$ symmetry has been studied in various complex optical structures, ongoing research persists in simpler configurations, such as dimers, trimers, and tetramers [40–42]. This focus may stem from the fact that these $\mathcal{PT}$-symmetric oligomers serve as fundamental building blocks for complex $\mathcal{PT}$-symmetric structures. Hence, elucidating the dynamics of these basic structures holds significant practical implications [43]. Multiple research teams have delved into the study of $\mathcal{PT}$-symmetric tetramer systems across diverse contexts [10,40,42,44–49], highlighting their pivotal role. This field represents a crucial extension of traditional Hermitian systems, attracting extensive research efforts. For instance, predictions have been made regarding the photon dynamics in optical pseudo-Hermitian systems composed of two waveguides [50] or two coupled cavities [51,52]. Subsequently, the dynamical behavior of mechanical resonators was probed in a mechanical $\mathcal{PT}$-symmetric quadruple-well hybrid optomechanical system [53]. Furthermore, the experimental realization of ultracold atoms in intricate optical lattices has been achieved [45,54–56]. Previous investigations on wave packet dynamics in these systems have revealed that the breaking of $\mathcal{PT}$ symmetry leads to the merging of energy bands, resulting in distinctive transport behaviors of both light and matter waves. These behaviors include birefringence, nonreciprocal diffraction, and bifurcation [57,58]. Additionally, reports have documented the occurrence of Bloch oscillations in extended $\mathcal{PT}$-symmetric lattices [59] and their subsequent dynamical behaviors [60]. Despite the recent significant advancements in this field, there remains an urgent need for a more thorough investigation of the pseudo-Hermitian characteristics and the accompanying dynamics within more generalized four coupled sites pseudo-Hermitian system. There remains a significant gap in our understanding of the phase transition, EPs, and dynamics of such system when non-Hermitian factors such as gain or loss are introduced. Given the rapid pace of technological development and the increasing demand for more efficient and robust quantum devices, the need for such a comprehensive study is both necessary and timely.

In this study, we address this knowledge gap by introducing a four coupled sites system that incorporates distinct pairs of gain and loss. The four coupled sites system exhibits a high degree of symmetry, which simplifies the theoretical analysis while retaining the essential features of pseudo-Hermitian systems. Furthermore, such a system can be engineered to exhibit tunable gain and loss, thereby inducing the desired pseudo-Hermitian behavior. This makes it an excellent model for experimentally studying the effects of pseudo-Hermiticity in a controlled setting. Our intention is to propose a theoretical model that captures the essential features of pseudo-Hermitian systems and to demonstrate the generality of our findings.

Our primary focus is on exploring the phase transition and dynamical characteristics of this system, aiming to contribute to the understanding of non-Hermitian quantum physics. By analytically deriving the pseudo-Hermitian condition and considering various structures of gain and loss within the quadruple wells, we classify the system into two distinct configurations. The phase transitions and EPs emerge in both types of symmetric systems, each exhibiting unique characteristics. Leveraging the phase diagram of eigenenergy, we numerically calculate the dynamic current of this quadruple-well system, finding it amenable to predicting properties of the energy spectrum. Our findings provide a potential avenue for investigating the pseudo-Hermitian characteristics, encompassing both phase transition and EPs. This study enhances our fundamental understanding of non-Hermitian quantum physics.

The paper is organized as follows. In Sec. II, we introduce the physical model of a four coupled sites system with controllable gain and loss. Using the general pseudo-Hermitian condition, we verify that the system uniquely supports two pseudo-Hermitian configurations: Configuration A, featuring equal-strength gain (loss) in diagonal wells, and Configuration B, featuring equal-strength gain (loss) in adjacent wells. In Sec. III, we study the phase transition and high-order EPs. There are three distinct phase regions: Phase I (exact $\mathcal{PT}$-symmetric phase), Phase II (partially broken $\mathcal{PT}$ phase), and Phase III (completely broken $\mathcal{PT}$ phase). The phase diagrams for the two distinct configurations are obtained. Finally, we analytically studied the dynamics of the system in Sec. IV, derived the dynamic current, and investigated the dynamical characteristics in different phase regions. Conclusions are presented in Sec. V.

II. PHYSICAL MODEL OF A FOUR COUPLED SITES SYSTEM: TWO PSEUDO-HERMITIAN CONFIGURATIONS WITH TUNABLE GAIN AND LOSS

We consider a four coupled sites system (or quadruple-well system), where the four distinct wells are labeled as 1, 2, 3, 4, respectively. The system can exhibits two distinct types of coupling mechanisms: the coupling strength K between first well (third well) and second well (fourth well) and the coupling strength J between second well (first well) and third well (fourth well). In a realistic scenario, it is crucial to account for the damping within the quadruple-well system [61]. Additionally, experimental manipulations can introduce a gain or loss [62,63]. Consequently, we incorporate gain or loss with strength γ_j into each potential well in our theoretical model, rendering it non-Hermitian. This non-Hermitian configuration is schematically illustrated in Fig. 1(a). Therefore, the Hamiltonian operator for this non-Hermitian system reads [64]

$$\hat{H} = -K(b_1^\dagger b_2 + b_3^\dagger b_4 + \mathrm{H.c.}) - J(b_2^\dagger b_3 + b_4^\dagger b_1 + \mathrm{H.c.}) + \mathrm{i}\sum_{j=1}^{4} \gamma_j b_j^\dagger b_j, \tag{1}$$

where $b_j^\dagger (b_j)$ is bosonic creation (annihilation) operator and $\gamma_j > 0$ ($\gamma_j < 0$) is the gain (loss) strength on the jth well. For convenience, we set $K = 1$ as the energy unit hereafter.

Taking the eigenstate of each well $\{|1\rangle, |2\rangle, |3\rangle, |4\rangle\}$ as the basis vector, the quantum state of the system can be expanded as

$$|\psi(t)\rangle = a_1(t)|1\rangle + a_2(t)|2\rangle + a_3(t)|3\rangle + a_4(t)|4\rangle, \tag{2}$$

where $a_j(t)$ $(j = 1, 2, 3, 4)$ are the time-dependent probability amplitudes. The dynamics of the system can be described by the Schrödinger equation, $\mathrm{i}d|\psi(t)\rangle/dt = \hat{H}|\psi(t)\rangle$. Hence,

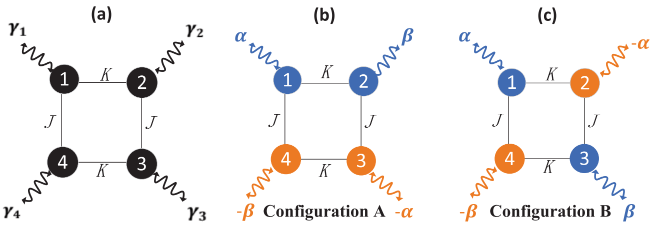

FIG. 1. (a) Schematic diagram of the four coupled sites system (or quadruple-well system) under consideration. The coupling strengths between the wells are designated as K and J, while γ_j signifies the gain or loss associated with the jth well. Notably, this system uniquely supports two distinct pseudo-Hermitian configurations, each exhibiting unique symmetries as depicted in (b) and (c). (b) In the pseudo-Hermitian configuration designated as Configuration A, considers equal gain (α) and loss ($-\alpha$) for the first well and third well, and equal gain (β) and loss ($-\beta$) for the second well and fourth well. (c) Alternatively, in the pseudo-Hermitian configuration labeled as Configuration B, considers equal gain (α) and loss ($-\alpha$) for the first well and second well, and equal gain (β) and loss ($-\beta$) for the third well and fourth well. These configurations highlight the versatility and complexity of non-Hermitian quantum systems, enabling the exploration of novel quantum phenomena and potential applications.

we can have the coupling equation of the probability amplitudes $a_j(t)\,(j = 1, 2, 3, 4)$ in each well as

$$\begin{aligned}
\mathrm{i}\frac{\mathrm{d}}{\mathrm{d}t}a_1(t) &= \mathrm{i}\gamma_1 a_1(t) - Ka_2(t) - Ja_4(t),\\
\mathrm{i}\frac{\mathrm{d}}{\mathrm{d}t}a_2(t) &= \mathrm{i}\gamma_2 a_2(t) - Ka_1(t) - Ja_3(t),\\
\mathrm{i}\frac{\mathrm{d}}{\mathrm{d}t}a_3(t) &= \mathrm{i}\gamma_3 a_3(t) - Ka_4(t) - Ja_2(t),\\
\mathrm{i}\frac{\mathrm{d}}{\mathrm{d}t}a_4(t) &= \mathrm{i}\gamma_4 a_4(t) - Ka_3(t) - Ja_1(t),
\end{aligned} \tag{3}$$

which dominated by an effective non-Hermitian Hamiltonian

$$H_{\mathrm{eff}} = \begin{pmatrix} \mathrm{i}\gamma_1 & -K & 0 & -J \\ -K & \mathrm{i}\gamma_2 & -J & 0 \\ 0 & -J & \mathrm{i}\gamma_3 & -K \\ -J & 0 & -K & \mathrm{i}\gamma_4 \end{pmatrix}. \tag{4}$$

Our primary emphasis is on elucidating the pseudo-Hermitian characteristics of this specific non-Hermitian system. It is a well-documented fact that any pseudo-Hermitian Hamiltonian exhibits eigenvalues that are either strictly real or exist as complex conjugate pairs [12,65,66]. Given this fundamental property, we proceed to analyze the secular equations, specifically expressed as $\mathrm{Det}(H_{\mathrm{eff}} - \lambda \mathrm{I}) = 0$, i.e.,

$$\begin{vmatrix} \mathrm{i}\gamma_1 - \lambda & -K & 0 & -J \\ -K & \mathrm{i}\gamma_2 - \lambda & -J & 0 \\ 0 & -J & \mathrm{i}\gamma_3 - \lambda & -K \\ -J & 0 & -K & \mathrm{i}\gamma_4 - \lambda \end{vmatrix} = 0, \tag{5}$$

and the complex conjugate expression $\mathrm{Det}(H^*_{\mathrm{eff}} - \lambda \mathrm{I}) = 0$, i.e.,

$$\begin{vmatrix} -\mathrm{i}\gamma_1 - \lambda & -K & 0 & -J \\ -K & -\mathrm{i}\gamma_2 - \lambda & -J & 0 \\ 0 & -J & -\mathrm{i}\gamma_3 - \lambda & -K \\ -J & 0 & -K & -\mathrm{i}\gamma_4 - \lambda \end{vmatrix} = 0, \tag{6}$$

should yield the same roots. Here, I represents the identity matrix. By expanding the determinants in Eq. (5) and Eq. (6) and subsequently comparing their respective coefficients, we deduce that the system parameters adhere to the following constraints:

$$\begin{aligned} \gamma_1 + \gamma_2 + \gamma_3 + \gamma_4 &= 0,\\ \gamma_1\gamma_2\gamma_3 + \gamma_1\gamma_2\gamma_4 + \gamma_1\gamma_3\gamma_4 + \gamma_2\gamma_3\gamma_4 &= 0. \end{aligned} \tag{7}$$

Hence, the non-Hermitian system described by Eq. (1) ought to fulfill the universal pseudo-Hermitian condition, which is formulated as follows:

$$\begin{matrix} \gamma_i = -\gamma_j = \alpha \\ \gamma_k = -\gamma_l = \beta \end{matrix}\ (i \neq j \neq k \neq l). \tag{8}$$

The constraint condition Eq. (8) necessitates the equilibrium between the total gain and total loss within the system. Guided by the derived pseudo-Hermitian condition Eq. (8), we strategically introduce gain and loss pairs at distinct sites of the quadruple-well system. Consequently, the system can be categorized into two distinct scenarios, depicted in Figs. 1(b) and 1(c), respectively labeled as Configuration A and Configuration B, based on their unique symmetry configurations.

In the pseudo-Hermitian configuration designated as Configuration A, as schematically illustrated in Fig. 1(b), identical gain and loss are imposed on opposing wells, respectively. Specifically, this involves introducing equal gain (α) and loss ($-\alpha$) in the first well and third well, respectively, while applying equivalent gain (β) and loss ($-\beta$) in the second well and fourth well, respectively. Consequently, the Hamiltonian can be reformulated to reflect these specific gain and loss configurations,

$$H^{(1)}_{\mathrm{eff}} = \begin{pmatrix} \mathrm{i}\alpha & -K & 0 & -J \\ -K & \mathrm{i}\beta & -J & 0 \\ 0 & -J & -\mathrm{i}\alpha & -K \\ -J & 0 & -K & -\mathrm{i}\beta \end{pmatrix}. \tag{9}$$

It is obvious that this Hamiltonian is pseudo-Hermitian and satisfies $\mathcal{PT}$ symmetry, whose $\mathcal{P}$ operator is [67]

$$\mathcal{P}^{(1)} = \begin{pmatrix} 0 & 0 & 1 & 0 \\ 0 & 0 & 0 & 1 \\ 1 & 0 & 0 & 0 \\ 0 & 1 & 0 & 0 \end{pmatrix}. \tag{10}$$

The time-reversal operator $\mathcal{T}$ is the complex conjugation operation defined as $\mathcal{T}i\mathcal{T}^{-1} = -i$.

Meanwhile, in the pseudo-Hermitian configuration designated as Configuration B, schematically depicted in Fig. 1(c), identical gain and loss are imposed on adjacent wells, respectively. Precisely, this involves introducing equal gain (α) and loss ($-\alpha$) in the first well and second well, respectively, while applying equivalent gain (β) and loss ($-\beta$) in the third well and fourth well, respectively. Notably, even in this configuration, the system retains its pseudo-Hermitian and $\mathcal{PT}$-symmetric properties, which can be expressed mathematically as

$$H_{\text{eff}}^{(2)} = \begin{pmatrix} \mathrm{i}\alpha & -K & 0 & -J \\ -K & -\mathrm{i}\alpha & -J & 0 \\ 0 & -J & \mathrm{i}\beta & -K \\ -J & 0 & -K & -\mathrm{i}\beta \end{pmatrix}. \tag{11}$$

The $\mathcal{P}$ operator for Eq. (11) is shown as [67]

$$\mathcal{P}^{(2)} = \begin{pmatrix} 0 & 1 & 0 & 0 \\ 1 & 0 & 0 & 0 \\ 0 & 0 & 0 & 1 \\ 0 & 0 & 1 & 0 \end{pmatrix}. \tag{12}$$

These configurations highlight the versatility and complexity of non-Hermitian quantum systems, enabling the exploration of novel quantum phenomena and potential applications.

III. PHASE TRANSITIONS IN PSEUDO-HERMITIAN SYSTEMS

A. Three phases

We now turn our attention to the phase transitions supported by the non-Hermitian system in the two pseudo-Hermitian configurations, namely Configuration A and Configuration B. Our focus is particularly on the influence of symmetry on these phase transitions. For the pseudo-Hermitian configurations in both the Configuration A and the Configuration B, the eigenvalues of the respective systems for these two scenarios are expressed as follows:

$$E = \pm\sqrt{\frac{\Delta_1 \pm \sqrt{\Delta_2}}{2}}. \tag{13}$$

The eigenvalues of the system in both Configuration A and Configuration B are parameterized by Δ_1 and Δ_2, which are defined as follows: for Configuration A, $\Delta_1 = 2J^2 + 2K^2 - \alpha^2 - \beta^2$ and $\Delta_2 = [4K^2 - (\alpha - \beta)^2][4J^2 - (\alpha + \beta)^2]$; while for Configuration B, $\Delta_1 = 2J^2 + 2K^2 - \alpha^2 - \beta^2$ and $\Delta_2 = 4J^2[4K^2 - (\alpha - \beta)^2] + (\alpha^2 - \beta^2)^2$. Both Δ_1 and Δ_2 encompass the entirety of the system's parameters, comprehensively reflecting their collective influence on the eigenvalues.

Based on Eq. (13), the system under investigation can be systematically classified into three distinct phases, each characterized by the interplay of two independent parameters, Δ_1 and Δ_2. Figure 2 presents a clear demarcation of these three phases on the (Δ_1, Δ_2) parameter plane, offering a comprehensive visualization of the system's phase diagram. (i) Phase I representing exact $\mathcal{PT}$-symmetric phase, where $\Delta_2 > 0$ and $\Delta_1 > \sqrt{\Delta_2}$, all four energy levels are real. (ii) Phase II defining partially broken $\mathcal{PT}$-symmetric phase, where $\Delta_2 > 0$ and $\Delta_1^2 < \Delta_2$, two energy levels are real $(\pm\sqrt{\Delta_1 + \sqrt{\Delta_2}})$, while the other two form a conjugate pair $(\pm\sqrt{\Delta_1 - \sqrt{\Delta_2}})$. (iii) Phase III corresponding to completely broken $\mathcal{PT}$-symmetric phase, where $\Delta_2 < 0$ or $\Delta_1 < 0$ and $\Delta_1^2 > \Delta_2 > 0$, all four energy levels exhibit conjugate pairs. The intricate structure of eigenvalues, as described by Eq. (13), demonstrates the profound impact of gain and loss on the system's eigenvalue landscape.

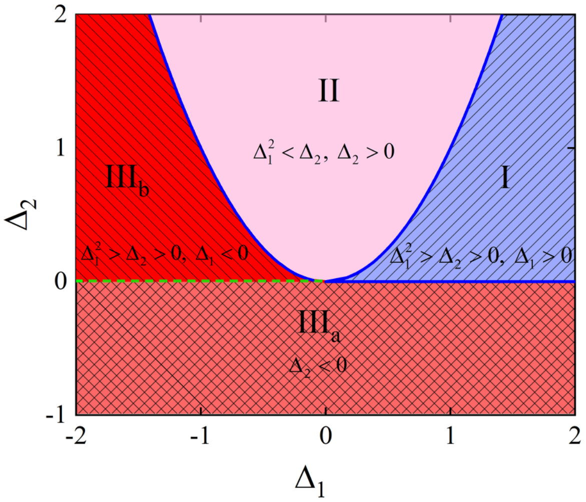

FIG. 2. The three distinct phases on the parameter plane $(\Delta_1,\ \Delta_2)$. When $\Delta_2 > 0$ but with $\Delta_1 > \sqrt{\Delta_2}$, all four energy levels are purely real, representing the exact $\mathcal{PT}$-symmetric phase, labeled as Phase I. Conversely, for $\Delta_2 > 0$ and $\Delta_1^2 < \Delta_2$, two energy levels remain real, whereas the remaining two form a complex conjugate pair, signifying the partially broken $\mathcal{PT}$-symmetric phase, denoted as Phase II. Lastly, for the conditions $\Delta_2 < 0$ or $\Delta_1 < 0$ with $\Delta_1^2 > \Delta_2 > 0$, all four energy levels exhibit two complex conjugate pairs, representing the completely broken $\mathcal{PT}$-symmetric phase, labeled as Phase III. The two solid blue lines correspond to exceptional lines (ELs) that are comprised of a series of second-order exceptional points (EP2). Notably, Phase III is further subdivided by a green dashed line ($\Delta_2 = 0$, $\Delta_1 < 0$) into Phase III_a and Phase III_b based on whether the real parts of the conjugate pairs are nonzero or zero, by the green dashed line.

The symmetry exhibited by the energy spectrum of the system around zero energy is intimately linked to the presence of a $\mathcal{PT}$ symmetric traceless matrix. To provide a clearer understanding of the system's phase transition, we have theoretically calculated and presented in Fig. 3 the real (E_r) and imaginary (E_i) parts of the eigenvalues in Configuration B. In this scenario, the prescribed gain and loss are applied to the first well and second well, while the third well and fourth well possess equal and adjustable gain or loss. As the gain or loss parameter (β) traverses from -3 to 3, the characteristics of the system's four energy levels undergo transformations, signifying the occurrence of a phase transition within the system. Figure 3 illustrates the energy spectrum diagram for distinct phase regions, highlighting the system's operation in three distinct phases. The solid blue line, dashed cyan line, dashed purple line, and dashed red line represent the four energy levels. The blue region corresponds to the exact $\mathcal{PT}$-symmetric phase, characterized by an entirely real spectrum (Phase I). The pink region represents the partially broken $\mathcal{PT}$-symmetric phase, featuring one pair of conjugate energy levels (Phase II). Finally, the red region signifies the completely broken $\mathcal{PT}$-symmetric phase, encompassing two pairs of conjugate energy levels (Phase III). Furthermore, the parameter space of β is partitioned into three sections. Notably, there exist second-order exceptional points (EP2) and fourth-order exceptional points (EP4), which correspond to the coalescing

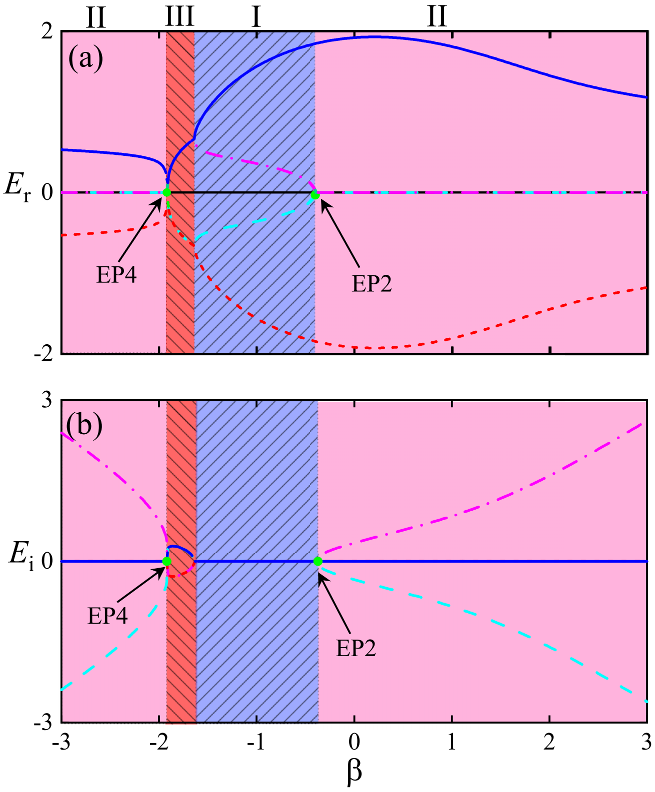

FIG. 3. The real (a) and imaginary (b) parts of the eigenvalue as a function of β for the pseudo-Hermitian configurations within Configuration B. The distinct regions represented by the blue, red, and pink areas correspond to the exact $\mathcal{PT}$-symmetric phase (labeled as Phase I), the partially broken $\mathcal{PT}$-symmetric phase (labeled as Phase II), and the completely broken $\mathcal{PT}$-symmetric phase (labeled as Phase III), respectively. Here, as examples, the parameters are set to $K = J = 1, \alpha = 0.657$.

of two and four energy levels, respectively. These EPs mark critical transitions within the system's phase structure.

B. Comparing phase transitions of two pseudo-Hermitian configurations with distinct symmetry

We now undertake a comparative analysis of phase transitions in two pseudo-Hermitian configurations (Configuration A and Configuration B), each exhibiting distinct symmetries. By scrutinizing the inherent characteristics of each configuration, our objective is to gain a profound understanding of the underlying mechanisms that govern these transitions. Thereby enhancing our understanding of the intricate interplay between symmetry, coupling, and phase transitions in non-Hermitian quantum systems.

Herein, we meticulously illustrate the phase transitions exhibited by two distinct pseudo-Hermitian configurations, namely Configuration A and Configuration B, across the comprehensive parameter space (J, α, β). Utilizing the real and imaginary components of the system's eigenvalues, the entire parameter space is meticulously partitioned into three regions: I, II, and III. These regions are characterized by their unique eigenspectra: Region I features four fully real eigenvalues, signifying the exact $\mathcal{PT}$-symmetric phase; Region II displays two real and two pure imaginary eigenvalues, indicative of the partially broken $\mathcal{PT}$-symmetric phase; and Region III exhibits four complex eigenvalues, marking the completely broken $\mathcal{PT}$-symmetric phase.

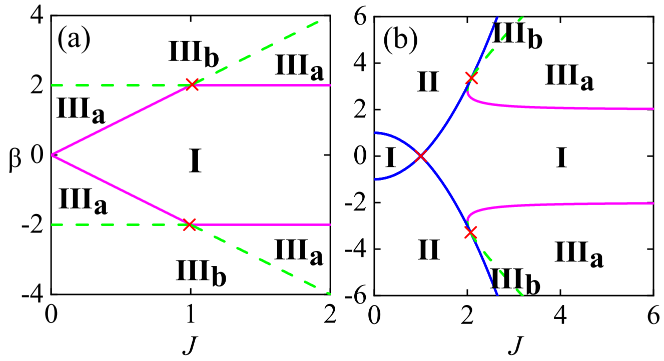

FIG. 4. Phase diagrams on the parameter plane $(J,\ \beta)$ for two distinct pseudo-Hermitian cases exhibiting different symmetry configurations, as depicted in (a) for Configuration A and (b) for Configuration B, respectively. These phase diagrams reveal three distinct phases that are clearly delineated by a series of exceptional lines, which correspond to EP2. Notably, the intersection points of two such exceptional lines represent EP4. It is evident that there are significant differences between the pseudo-Hermitian scenarios with different symmetry configurations. Regions I, II, and III are the exact $\mathcal{PT}$-symmetric phase, the partially broken $\mathcal{PT}$-symmetric phase, and the completely broken $\mathcal{PT}$-symmetric phase, respectively. The blue solid curve represents the EP2 with one defective eigenstate, the purple solid and the green dashed curves indicate the EP2 with two defective eigenstates; the dashed green curve divides region III into two subregions $\mathrm{III_a}$ and $\mathrm{III_b}$, where the real part of eigenvalues are nonzero and zero. The red cross marks the higher order EP4, indicating that the intersection of two types of EP2 curves. Here, the parameters $\alpha = 0$ and $K = 1$.

It is noteworthy that within Region III, there may exist subregions characterized by either four purely complex spectra or four purely imaginary spectra. For the sake of clarity and discussion, these subregions are designated as Phase $\mathrm{III_a}$ and Phase $\mathrm{III_b}$, respectively. The boundaries demarcating these phase regions are determined by Eq. (13), which defines the exceptional lines. These lines encompass EP2, and the intersection of two such ELs represents an EP4, a higher-order exceptionality.

In Fig. 4, the phase diagrams are plotted on the parameter plane $(J,\ \beta)$ for two distinct pseudo-Hermitian configurations, each exhibiting unique symmetry configurations. Specifically, Fig. 4(a) represents Configuration A while Fig. 4(b) corresponds to Configuration B. These diagrams clearly depict three distinct phases, delineated by a series of ELs that correspond to EP2. Notably, the intersection points of two such ELs represent EP4, a higher-order exceptional point. The exceptional curves demarcate the transitions between distinct phases. Specifically, the purple solid line and green dashed line correspond to $\Delta_2 = 0$ in Eq. (13), signifying the emergence of a pair of two-state merging EP2. These lines serve as the boundary separating regions I and III, where the $\mathcal{PT}$ symmetry is broken in zone III. The green dashed curve, in particular, designates the dividing line between regions characterized by complex and purely imaginary eigenvalues in Fig. 4(a).

In Fig. 4(b), the blue solid curve results from the condition $\Delta_1^2 = \Delta_2$, which marks the presence of another two-state EP2. This curve defines the transition from the $\mathcal{PT}$-symmetric phase in region I to the partially broken $\mathcal{PT}$-symmetric phase in region II. The red cross indicates the intersection point of two exceptional curves, representing the coalescence of two pairs of two-state energy levels into a single EP4. By leveraging the phase diagram depicted in Fig. 4, we are able to predict the critical conditions for the existence of $\mathcal{PT}$-symmetric and broken $\mathcal{PT}$-symmetric phases within the pseudo-Hermitian model. This analysis provides a comprehensive understanding of the phase transitions and EPs in this non-Hermitian quantum system.

For Configuration A, the critical points for the phase transition between real spectra and complex spectra are given by $\Delta_2 = 0$ ($\mathcal{PT}$ broken phase transition point). For $\alpha = 0$ [as shown in Fig. 4(a)], which can be expressed as

$$\beta_{c1}^{(1)} = \pm 2J \ \ (\text{or} \ \ = \pm 2K). \tag{14}$$

When β reaches the critical value of β_{c1}, the system enters an EP2 state, exhibiting a pair of two-state coalescence. In this state, the central two levels merge, resulting in the emergence of two defect eigenstates. The spectrum of these eigenstates consists of merged conjugate pairs. Notably, under the condition $J = J_{c1} = K$, the critical value of β_{c1} is given by $\pm 2K$. When this condition is satisfied, all four levels of the system coalesce, indicating that the system transitions to an EP4 state. On the other hand, when $\Delta_1^2 = \Delta_2 \neq 0$, the equation lacks a solution. Consequently, the system in the Configuration A does not exhibit a phase transition boundary between fully real spectra, partially real spectra, and partially real spectra merging with fully complex spectra. As a result, the system lacks a Phase II in this scenario.

For Configuration B, the phase transition between real and complex spectra is also characterized by critical points derived from the condition $\Delta_2 = 0$. Specifically, considering the case where $\alpha = 0$ as depicted in Fig. 4(b), the critical points are expressed as

$$\beta_{c1}^{(2)} = \pm\sqrt{2}\sqrt{J^2 \pm \sqrt{J^2(J^2 - 4K^2)}}. \tag{15}$$

When J attains the critical value of $J_{c1} = 2K$, a remarkable phenomenon occurs: the four energy levels coalesce, indicating that the system transitions to an EP4 state. On the other hand, when $\Delta_1^2 = \Delta_2 \neq 0$, a distinct behavior is observed. In this scenario, the two central energy levels merge at $E = 0$, signifying the emergence of an EP2 state with two-state coalescence. This state is accompanied by the presence of a defective eigenstate. Furthermore, the critical conditions for the balance between gain and loss are given by

$$\beta_{c2}^{(2)} = \pm\frac{J^2 - K^2}{K}. \tag{16}$$

Notably, when J attains another critical value of $J_{c2} = K$, the four energy levels once again coalesce, signifying that the system transitions to an EP4 state. These findings provide crucial insights into the phase behavior and critical conditions of the system in Configuration B.

Next, we delve into the scenario where $\alpha \neq 0$. In this scenario, all four wells of the system experience either gain or loss. To gain insights into the system's behavior, we present phase diagrams in the (α, β) parameter plane for both Configuration A (top row) and Configuration B (bottom row). These diagrams are plotted for various values of J (ranging from $J = 0.5, J = 1$, to $J = 2$, from left to right). The phase diagram regions depicted in these figures exhibit similarities to those shown in Fig. 5. The curves within these diagrams represent boundaries that delineate distinct phases. Specifically, the green and blue curves correspond to $\Delta_2 = 0$, signifying the occurrence of a pair of two-state coalescences in an EP2 state. Furthermore, the solid blue curve indicates $\Delta_1^2 = \Delta_2$, which represents the merging of two states in an EP2 state. Crucially, the intersections of these curves represent EP4 states, marking points where the system exhibits a higher-order EP. These phase diagrams provide a comprehensive understanding of the system's behavior in the presence of gain and loss and highlight the critical conditions leading to different types of EPs.

The critical conditions for phase transitions can be derived for both Configuration A and Configuration B. In the Configuration A, the transition between the real and complex spectra occurs precisely when $\Delta_2 = 0$. This condition translates to the following critical points:

$$\beta_{c1}^{(1)} = \pm 2J - \alpha, \ \text{and} \ \pm 2K + \alpha. \tag{17}$$

At this critical point, the system enters an EP2 state, characterized by a pair of two-state coalescences. This coalescence results in the merging of the two spectra above and below the critical point, leading to the emergence of two defective eigenstates with a spectrum consisting of a merged conjugate pair. Notably, in this scenario, the system does not exhibit a Phase II, as evident in Figs. 5(a)–5(c).

On the other hand, when $\Delta_1^2 = \Delta_2 \neq 0$, a unique phenomenon occurs. The two central energy levels converge at $E = 0$, creating a two-state merging EP2 system. This merging is accompanied by the emergence of a defect eigenstate. The critical gain and loss parameters that satisfy this condition are given by

$$\beta_{c2}^{(1)} = -K + \frac{J^2}{K + \alpha}, \ \text{and} \ K + \frac{J^2}{-K + \alpha}. \tag{18}$$

For the Configuration B, the equation governing the critical curves is more intricate. Therefore, we omit the explicit form here but emphasize that similar critical conditions exist in this model, albeit with a more involved mathematical description. However, it is worth noting that the analysis of these critical conditions provides crucial insights into the phase transitions and EPs behavior in non-Hermitian quantum systems.

IV. DYNAMIC CURRENT OF PSEUDO-HERMITIAN SYSTEM

In this section, we systematically investigate the dynamics within pseudo-Hermitian systems, focusing particularly on elucidating the dynamical characteristics across distinct phase regions.

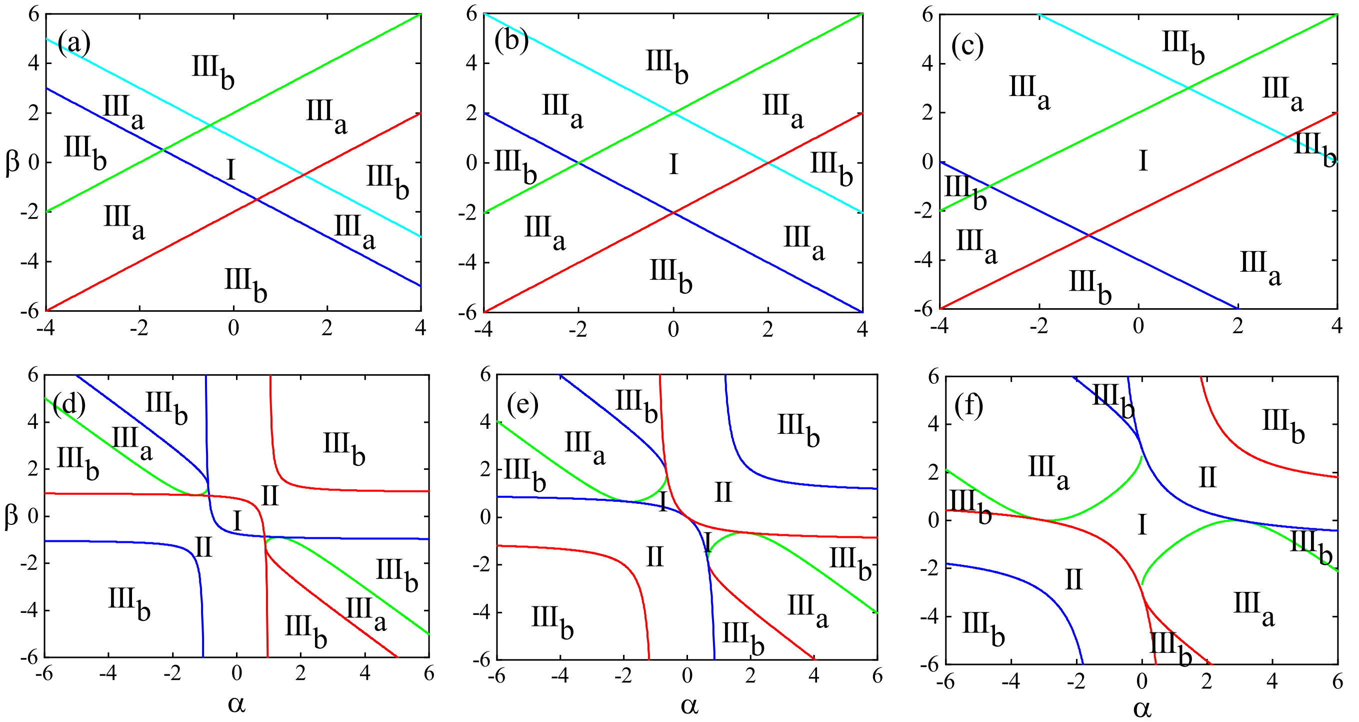

FIG. 5. Phase diagram in the parameter space (β, α) is presented for both Configuration A (top panel) and Configuration B (bottom panel). The regions labeled as I, II, $\mathrm{III_a}$, and $\mathrm{III_b}$ correspond to the phases indicated in Fig. 4, ensuring consistency in notation. Notably, the intersection points discernible within these diagrams signify the presence of an EP4. At these precise intersections, the matrix possesses a single eigenvector. The parameters used in the diagrams are $J = 0.5$ for (a), (d), $J = 1$ for (b), (e), and $J = 2$ for (c), (f), respectively. These phase diagrams provide a comprehensive understanding of the system's behavior across different parameter ranges in both Configuration A and Configuration B. Here, the parameter $K = 1$.

A. Probability amplitudes in distinct phases

Both Configuration A and Configuration B possess linear characteristics, allowing for analytical solutions. The probability amplitudes, as defined in Eq. (2), can be derived by incorporating their respective initial conditions. Assuming an initial preparation in the first well, i.e., $|\psi(0)\rangle = [1,\ 0,\ 0,\ 0]^T$, the analytical expressions for the probability amplitudes in both Configuration A and Configuration B are detailed in Appendix. Additionally, numerical solutions of Eq. (3) can be obtained, providing further insights into the system's dynamics. Consequently, the population distribution within the system is visualized in Fig. 6.

Initially, a loss and a gain are imposed on the first well and second well, respectively, with β set to 3. In this configuration, the system resides in the completely broken $\mathcal{PT}$-symmetric Phase $\mathrm{III_b}$. As β is gradually incremented, the system transitions to Phase $\mathrm{III_a}$. However, it should be noted that the dynamics in both these phases remain unstable and divergent. This instability stems from the fact that Phase $\mathrm{III_b}$ exhibits a purely imaginary energy spectrum, causing exponential divergence [shown in Fig. 6(a)], whereas Phase $\mathrm{III_a}$ possesses a complex conjugate pair of eigenvalues, leading to oscillatory divergence [as shown in Fig. 6(b)].

A significant transition occurs when β reaches 1, marking the transition to the exact $\mathcal{PT}$-symmetric Phase I. Within this phase, the system exhibits stable dynamics, oscillating in a quasiperiodic manner as depicted in Fig. 6(c). Of particular interest is the propagation characteristics within the partially broken $\mathcal{PT}$-symmetric phase. Here, a key feature is the exponentially growing dynamics superimposed with oscillations, stemming from the imaginary and real parts of the eigenvalues, respectively, as evident in Fig. 6(d).

The aforementioned analysis underscores the potential of engineering $\mathcal{PT}$ symmetry for quasistable propagation of appropriately emitted wave packets. Even in the stationary dynamics of the $\mathcal{PT}$-broken phase, such propagation can be parametrically tuned based on the choice of loss-gain parameters. This tunable nature offers intriguing possibilities for controlling and manipulating quantum systems in non-Hermitian settings.

B. Dynamic current in distinct phases and EPs

Here, we derive an expression for the dynamic current circulating around the four-site loop, as schematically illustrated in Fig. 1(a). Employing the continuity equation at each site within the four-potential well system, we obtain the relevant expression for the current flow. Notably, the specific form of the continuity equation at the nth site involves the intricate interplay between the wave functions and their associated dynamics [68,69], leading to the expression,

$$\partial_t (b_n^\dagger b_n) = \mathrm{i}[b_n^\dagger b_n, \hat{H}] = I_{n,n+1} - I_{n-1,n}, \tag{19}$$

where the Hamiltonian operator $\hat{H}$ is given by Eq. (1). This expression encapsulates the essential physics governing the current flow within the four-site loop and serves as a crucial

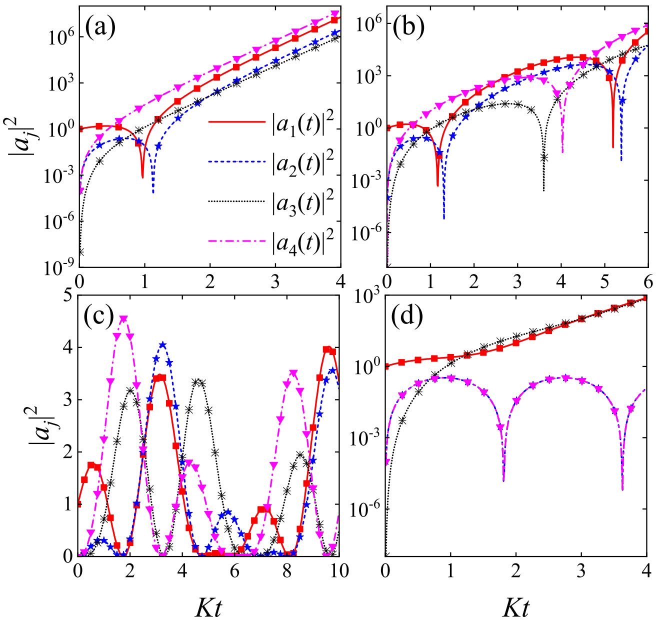

FIG. 6. The dynamics of probability amplitudes $|a_j(t)|^2$ ($j = 1, 2, 3, 4$) in each well within the pseudo-Hermitian Configuration B. Specifically, (a), (b), (c), and (d) present the temporal evolution of these amplitudes in Phase III$_b$, Phase III$_a$, Phase I, and Phase II, respectively, corresponding to distinct values of β ($-3, -2, -0.8$, and 1). The other relevant parameters are fixed at $K = J = 1$, and $\alpha = 1$. The lines and points depicted in the figure represent the numerical and analytical results, respectively, and they align perfectly with each other, validating the consistency of our calculations and the accuracy of our methods. This comprehensive analysis allows for a deeper understanding of the dynamical characteristics in different phase regions within the pseudo-Hermitian framework.

component in our analysis. In Eq. (19), we have introduced the local dynamic current operator $I_{n,n+1}$, which accounts for the transfer of excitations between two adjacent sites n and $n+1$ (we assume modular arithmetic for the site numbers),

$$I_{n,n+1} = -\mathrm{i}g(b_n^\dagger b_{n+1} - b_{n+1}^\dagger b_n), \tag{20}$$

where g is the coupling strength between well, for example, $g = K$ for $n = 1$, 3 and $g = J$ for $n = 2$, 4. Here, we have used cyclic boundary conditions, corresponding to the quadrilateral geometry sketched in Fig. 1(a).The bosonic creation (annihilation) operators of the system are denoted by $b_n^\dagger$ (b_n), and $b_5 = b_1$. Similarly, the dynamic particle current operator of the system can be defined as

$$I = I_{1,2} + I_{2,3} + I_{3,4} + I_{4,1}. \tag{21}$$

Notably, the particle current definition of Eq. (19) does not explicitly depend on the loss and gain in the system, instead, these features enter the consideration indirectly through the operators $a_n^* a_{n+1}$. We denote the dynamic current of the whole system as

$$\begin{aligned}\langle I\rangle = &-iK[a_2(t)a_1^*(t) + a_4(t)a_3^*(t) - \text{c.c.}]\\ &- iJ[a_1(t)a_4^*(t) + a_3(t)a_2^*(t) - \text{c.c.}]. \end{aligned}\tag{22}$$

Hence, the dynamic current I in different phases of the $\mathcal{PT}$-symmetric quadruple-well potential can be obtained by numerical and analytical methods according to the dynamics of the system.

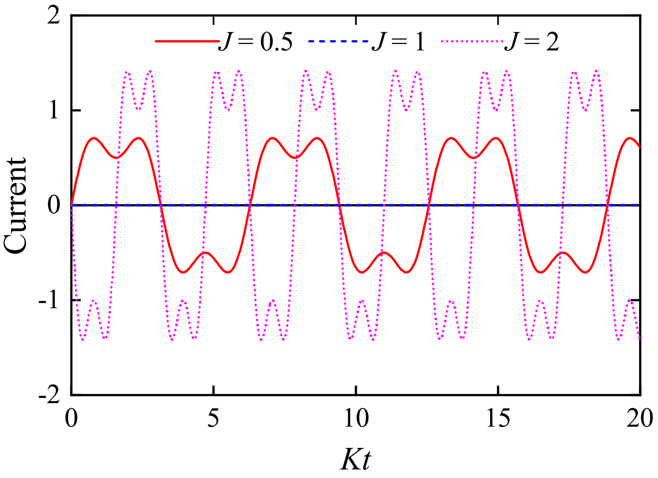

FIG. 7. The dynamic current I in the Hermitian scenario ($\alpha = \beta = 0$). The red solid, blue dashed, and magenta dotted curves for $J = 0.5$, $J = 1$, and $J = 2$, respectively.

For comparative purposes, in Fig. 7, we initially illustrate the dynamic current in the Hermitian scenario, where ($\alpha = \beta = 0$). Under this condition, the dynamic current exhibits periodic characteristics, and the time-averaged current is zero. The direction of the dynamic current is determined by the magnitudes of K and J. Specifically, when ($J < K$) (for instance, ($J = 0.5$)), the dynamic current proceeds in a clockwise direction. Conversely, for ($J > K$) [i.e., ($J = 2$)], the current is counterclockwise. Notably, when ($J = K$), the dynamic current fails to form. These observations provide a basis for effectively regulating the periodicity, amplitude, and direction of the dynamics.

Now, we turn our attention to exploring the dynamic current in the non-Hermitian scenario. To elucidate the distinguishing features of the dynamical current I in Phase I, particularly its dependence on the parametric gain and loss strengths, as well as the coupling strength, we direct our attention to the parameter space within the phase diagram of Configuration A, prominently displayed in the top panel of Fig. 5. The manifestation of the dynamical current I in Phase I is illustrated in Fig. 8. By modulating the gain-loss intensity β in the second and fourth wells, while keeping constant the loss-gain parameter α in the first and third wells, as well as the coupling strength J, we observe that the system operates within Phase I. In this regime, the dynamical current exhibits quasiperiodic oscillatory patterns, with a notable increase in the amplitude of these oscillations as the gain-loss intensity β is progressively enhanced. This phenomenon is clearly demonstrated in Fig. 8(a). The time-averaged current in the exact $\mathcal{PT}$ symmetric phase is close to zero.

Meanwhile, the current is a function of coupling amplitude J. Here, the gain-loss parameters α and β are fixed and the system works in Phase I. Hence, the dynamic current under different coupling J is obtained in Fig. 8(b). At first, the coupling will not change the quasiperiodicity regardless of the coupling J, but the strong coupling will protect the periodicity of the dynamic current shown in Fig. 8(b). The amplitude of

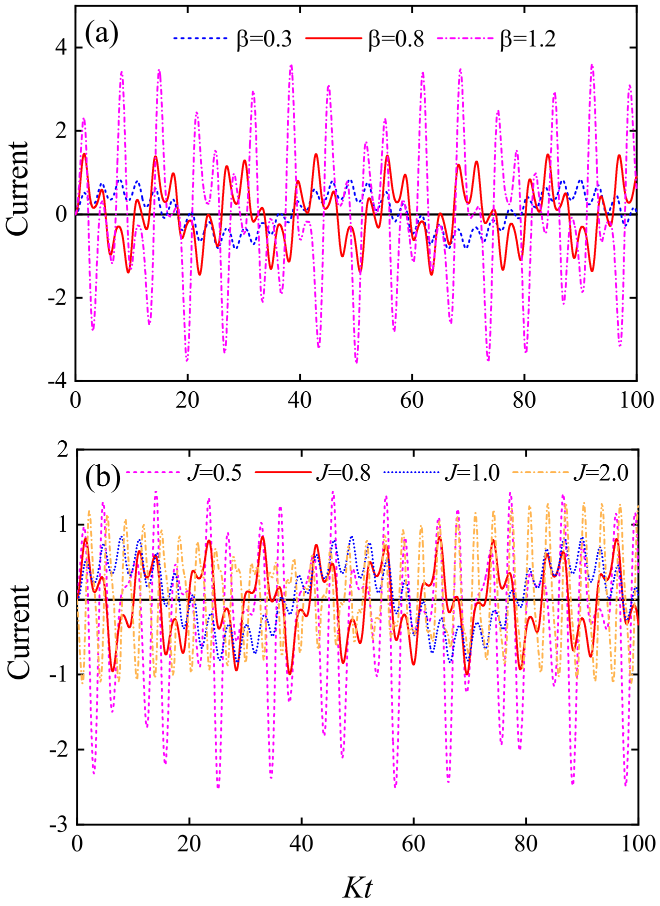

FIG. 8. The dynamic current I in the exact $\mathcal{PT}$ symmetric phase. (a) The dynamic current I for various values of β, while fixing $\alpha = 0.5$ and $J = 1$. The red solid, blue dashed, and magenta dotted curves for $\beta = 0.3$, $\beta = 0.8$, and $\beta = 1.2$, respectively. (b) The dynamic current I for various values of coupling J, while fixing $\alpha = 0.0$ and $\beta = 0.5$. The red solid, blue dashed, and magenta curves, and orange dashed for $J = 0.5$, $J = 0.8$, and $J = 1.0$, and $J = 2.0$, respectively.

dynamic current will decrease with the increment of coupling J also. For example, $J < 1$, the dynamic current direction is shifted in the negative direction, and $J > 1$, the current direction is offset in the positive direction. Note that when $\alpha = \beta$ ($\alpha = -\beta$), the dynamic current is evenly distributed between the positive and negative ends of the axis without offset. Therefore, the current in Phase I is stable and quasiperiodic shown in Fig. 8. The peak value of the current increases with the increase of β, and the larger the value of J, the smaller the peak value of the current. The oscillation period is not affected by the coupling parameter J.

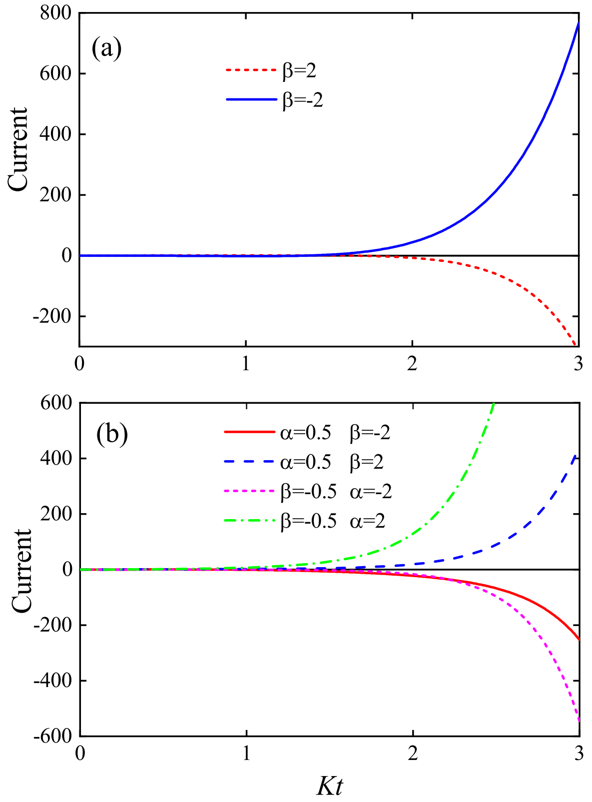

FIG. 9. Dynamic current I as a function of time t, in the partially broken $\mathcal{PT}$-symmetric phase example with Configuration B. (a) $J = 1$ and $\alpha = 0.5$, the dashed blue line is $\beta = 2$, and the solid red line is $\beta = 2$. (b) $J = \frac{1}{2}$, the solid red line is $\alpha = 0.5$ and $\beta = -2$, the dashed blue line is $\alpha = 0.5$ and $\beta = 2$, the dotted magenta line is $\alpha = -0.5$ and $\beta = -2$, and the dotted green line is $\alpha = -0.5$ and $\beta = 2$.

The dynamic current in the partially broken $\mathcal{PT}$-symmetric phase is also an important aspect of this system. When we take values of α and β in the Phase II region in Figs. 5(e) and 5(f). Figure 9 shows that the dynamic current is unstable and the size of the dynamic current increases exponentially with time. Larger gain or loss strength and coupling strength lead to a faster change rate of current. When $J \geqslant 1$, the direction of dynamic current in Phase II region is directly related to the phase diagram region. It is worth mentioning that when $J = \beta = \alpha = 1$, the dynamic current is always equal to zero. In the phase figure Fig. 5(e), we take the diagonal line $\alpha = \beta$ as the boundary and take the value above the diagonal boundary, and the direction of the current is positive (clockwise along the well $1 \rightarrow 2 \rightarrow 3 \rightarrow 4$). For example, when $\beta = 2$, the corresponding blue solid line is shown in Fig. 9(a). When α and β are below the diagonal line, the dynamic current is negative (counterclockwise along the well $4 \rightarrow 3 \rightarrow 2 \rightarrow 1$). For example, when $\beta = -2$, the corresponding red dashed line is shown in Fig. 9(a). It is worth noting that when $J < 1$, the direction of the current is not directly related to the phase diagram region, but only shows correlation in some regions shown as Fig. 9(b). Taking the system in Fig. 5(f) for example, here, $J = \frac{1}{2}$, and others are selected as $\alpha = 0.5$, $\beta = \pm 2$ and $\alpha = -0.5$, $\beta = \pm 2$ for dynamic current, respectively. Hence, the direction of the current is not uniform shown in Fig. 9(b) above the diagonal $\alpha = \beta$ in the phase diagram Fig. 5(f). This is not consistent with the result for $J \geqslant 1$.

When the system works in region Phase III, the dynamic current is in Fig. 10, we depict the dynamics current I of the system when it is in the $\mathcal{PT}$ symmetry fully broken Phase III. Obviously, it shows a completely different behavior compared with the case in the $\mathcal{PT}$-symmetric phase. As shown in Fig. 10(a), when $\alpha = 2$, $\beta = -2$, the system has four complex energy eigenvalues, and in general, the eigenstate strength

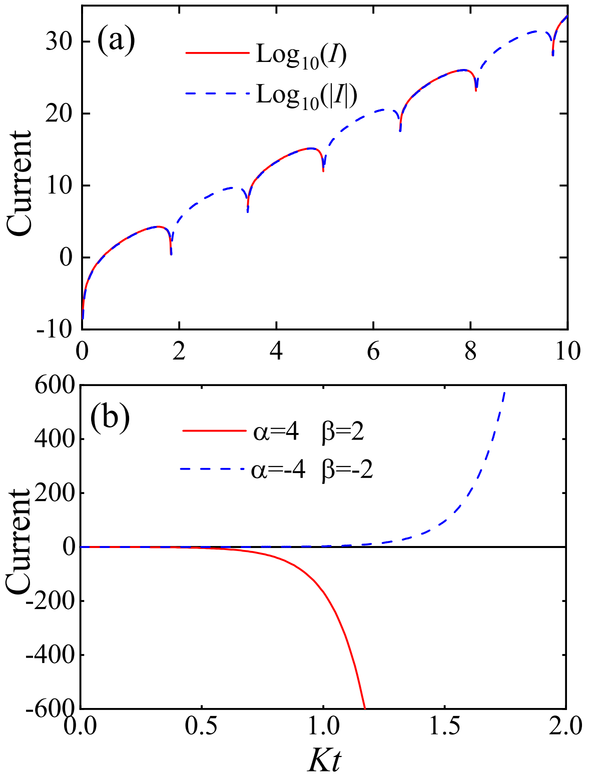

FIG. 10. Dynamic current I as a function of time t, in the completely broken $\mathcal{PT}$-symmetric phase for Configuration B. (a) Log image of the current over time in region Phase III$_\mathrm{a}$ with $\alpha = 2$ and $\beta = -2$. The part where the red solid line and the blue dashed line coincide means that the direction of the current is positive, and only the blue dashed line means that the direction of the current is negative. (b) Dynamic current as a function of time in region Phase III$_\mathrm{b}$, the solid blue line is $\alpha = -4$ and $\beta = -2$, the dashed red line is $\alpha = 4$ and $\beta = 2$. Other parameters $J = 1$.

increases and oscillates with time. The oscillation is caused by four distinct eigenstates (with a real energy part), while the increase in intensity is caused by having an intrinsic energy (with an imaginary energy part). As a result, the dynamic current in the Phase III$_\mathrm{a}$ is oscillatory and the amplitude of the oscillations gradually increases over time.

As shown in Fig. 10(a), the overlap of the red and blue dashed lines represents the positive dynamic current, while only the blue dashed line represents the negative. In region Phase III$_\mathrm{b}$, the current variation characteristics are the same as in region Phase II. If two set parameters $\alpha = 4$, $\beta = 2$ and $\alpha = -4$, $\beta = -2$ are set, the dynamic current is presented in Fig. 10(b).

The examination of the dynamic current at EP is crucial for understanding the system's behavior in non-Hermitian quantum physics. Figure 11 illustrates the distinct characteristics of the dynamic current at EP. In the $\mathcal{PT}$-symmetric phase, the dynamic current exhibits quasiperiodic oscillations, indicative of the system's stability. Conversely, in the broken $\mathcal{PT}$-symmetric phase, the current diverges with monotone exponential growth, reflecting the system's instability.

Notably, within the complex energy spectrum (Phase III$_\mathrm{a}$), the dynamic current not only diverges but also oscillates,

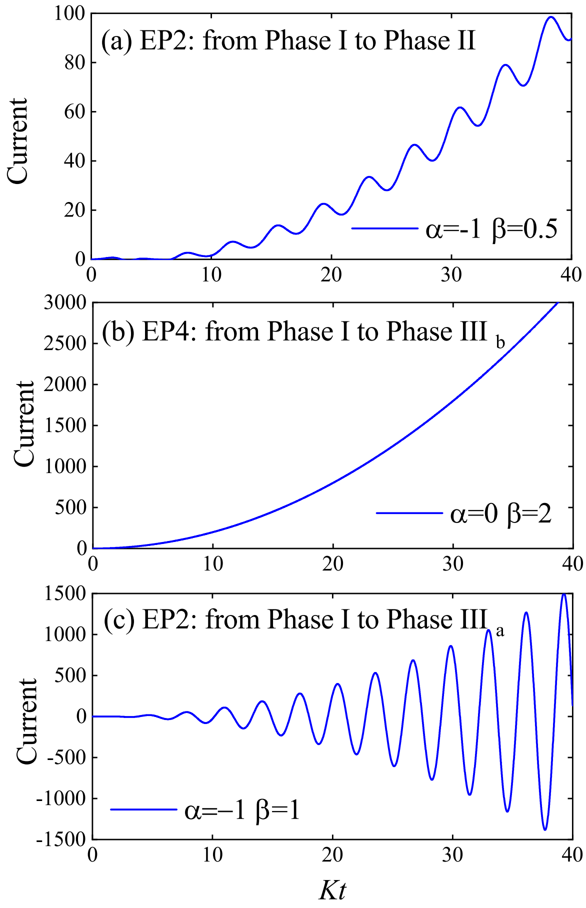

FIG. 11. The dynamic current behavior at EPs. (a) EP2 for transition from Phase I to Phase II (taking $\alpha = -1$, $\beta = 0.5$ as an example). (b) EP4 for transition from Phase I to Phase III$_\mathrm{b}$ (taking $\alpha = 0$, $\beta = 2$ as an example). (c) EP2 for transition from Phase I to Phase III$_\mathrm{a}$ (taking $\alpha = -1$, $\beta = 1$ as an example). The coupling parameter $J = 1$. These figures provide a comprehensive overview of the dynamic current's behavior at EPs, illustrating how it varies across different phase transitions and parameter settings.

demonstrating a unique combination of behaviors. As the EP is approached, the branches of the spectrum coalesce, ultimately becoming pairwise doubly degenerate at the EP. This degeneracy is characterized by a single oscillation frequency, underlying the system's unique dynamical response.

At the EP, where exponential growth and oscillation overlap (transitions from Phase I to Phase II and from Phase I to Phase III$_\mathrm{b}$), the rapid oscillation persists. However, the negative imaginary part of the energy spectrum introduces an exponential growth component to the dynamic current. This combined behavior is clearly observed in Figs. 11(a) and 11(b), where the exponential growth of the oscillation is evident.

In contrast, within the complex energy spectrum Phase III$_\mathrm{a}$, the dynamic current oscillates rapidly, and its amplitude increases significantly, as depicted in Fig. 11(c). This increase in amplitude highlights the enhanced oscillatory behavior in this phase, providing further insights into the system's dynamics in the presence of an EP. The analysis of the dynamic current at EPs offers a comprehensive understanding of the system's behavior in different phases, particularly in the complex energy spectrum, where the interplay between oscillation and exponential growth is pronounced.

It is imperative to clarify that the characteristics of the dynamic current in the same phase, regardless of the two pseudo-Hermitian scenarios, are indeed congruous. Consequently, in the aforementioned context, we have chosen to exemplify only one of the two pseudo-Hermitian scenarios.

V. CONCLUSIONS

We delved into the intricate behavior of a non-Hermitian quadruple-well potential. By introducing two pairs of gain and loss mechanisms, we have unlocked additional degrees of freedom that significantly enhance our ability to manipulate $\mathcal{PT}$ phase transitions and engender higher-order EPs. Exceptional points are significant in non-Hermitian systems and can lead to unique physical phenomena [29]. The occurrence of a third-order EPs for a pseudo-Hermitian cavity optomechanical system has been explored [20,21]. A pivotal aspect of our investigation lies in the derivation of a universal pseudo-Hermitian condition for this quadruple-well potential system. We definitively establish that the system uniquely supports two distinct pseudo-Hermitian configurations, each exhibiting distinct symmetries. This condition serves as a gateway to understanding how such a non-Hermitian system can exhibit both $\mathcal{PT}$-symmetric and broken $\mathcal{PT}$-symmetric behaviors, along with the occurrence of high-order EPs (EP4), in both configurations.

When considering symmetric wells with identical gain or loss characteristics, our analysis reveals that the system is confined to displaying exactly $\mathcal{PT}$-symmetric phase (Phase I), characterized by entirely real eigenvalues, or completely broken $\mathcal{PT}$-symmetric phase (Phase III), marked by the presence of solely complex eigenvalues. However, the situation becomes far more intricate when adjacent wells share the same gain or loss. In such scenarios, the system not only manifests the aforementioned exactly $\mathcal{PT}$-symmetric and completely broken $\mathcal{PT}$-symmetric phases but also exhibits an intermediary phase (Phase II), distinguished by the coexistence of two real eigenvalues and a pair of complex conjugate imaginary eigenvalues. Crucially, the phase regions of the system can be meticulously classified based on the spectra of the real and imaginary components of the Hamiltonian's eigenvalues. This classification provides a comprehensive road map for understanding the system's behavior across different parameter configurations. Furthermore, by presenting phase diagrams encompassing the entire parameter space, we offer a comprehensive visualization of how coupling constants and gain or loss intensities influence $\mathcal{PT}$ phase transitions.

Moreover, our investigation extends to the dynamic currents in proximity to various phase regions and EPs. In the precisely $\mathcal{PT}$-symmetric phase (Phase I), we observe stable quasiperiodic oscillations, reflecting the system's robustness against perturbations. In contrast, broken $\mathcal{PT}$-symmetric phase (Phase III) exhibit a more complex dynamical landscape, with stable oscillations coexisting with exponential growth, driven by the real and imaginary parts of the energy levels, respectively. Finally, in the completely broken $\mathcal{PT}$-symmetric phase, Phase $\mathrm{III_a}$ displays exponentially increasing oscillations, while Phase $\mathrm{III_b}$ is characterized by an even more drastic exponential divergence. The dynamic current exhibited at EPs demonstrates distinctive behavior during transitions between various phases. We should emphasize that the various dynamic currents arise without imparting nonreciprocal characteristics to the system. This observation highlights the profound influence of gain and loss on the system's dynamics, encompassing even nonreciprocal transport phenomena. This intriguing phenomenon holds immense potential for practical applications and has garnered considerable attention. For instance, recent studies have focused on the nonreciprocal transport with imbalanced on-site gain and loss [70,71]. The intricate interplay between gain, loss, phase transitions, and dynamics elucidated in this study deepens our understanding of non-Hermitian quantum systems, while also offering valuable insights into the design and manipulation of novel quantum phenomena in various fields including photonics and quantum systems.

ACKNOWLEDGMENT

This work was supported by the National Natural Science Foundation of China (Contracts No. 12005173 and No. 12365004) and by the Natural Science Foundation of Gansu Province (Contract No. 20JR10RA082).

APPENDIX: ANALYTICAL SOLUTION OF PROBABILITY AMPLITUDES

The analytical solutions of Eq. (2) in Configuration A under the initial condition $|\psi(0)\rangle = [1,\ 0,\ 0,\ 0]^T$ is expressed as

$$a_1(t) = (C_4 - C_1)\sinh(\theta_1) + (C_3 - C_2)\sinh(\theta_2) + (C_1 + C_4)\cosh(\theta_1) + (C_2 + C_3)\cosh(\theta_2),$$

$$a_2(t) = \frac{iK(\alpha+\beta)}{B}[\cosh(\theta_1) - \cosh(\theta_2)] + D_1\sinh(\theta_1) + D_2\sinh(\theta_2), \quad a_3(t) = \frac{(2JK)}{B}[\cosh(\theta_2) - \cosh(\theta_1)],$$

$$a_4(t) = \frac{iJ(\alpha-\beta)}{B}[\cosh(\theta_1) - \cosh(\theta_2)] + D_3\sinh(\theta_1) + D_4\sinh(\theta_2).$$

Here $A = \alpha^2 + \beta^2 - 2J^2 - 2K^2$, $B = \sqrt{4J^2 - (\alpha+\beta)^2}\sqrt{4K^2 - (\alpha-\beta)^2}$, $\theta_1 = \frac{t\sqrt{A+B}}{\sqrt{2}}$, $\theta_2 = \frac{t\sqrt{A-B}}{\sqrt{2}}$,

$$C_1 = \frac{(\sqrt{2}\sqrt{A+B} - 2\alpha)(\alpha^2 - \beta^2 + B) + 4J^2(\alpha-\beta) + 4K^2(\alpha+\beta)}{4B\sqrt{A+B}},$$

$$C_2 = \frac{(2\alpha - \sqrt{2}\sqrt{A-B})(-\alpha^2 + \beta^2 + B) + 8J^2(\alpha-\beta) + 8K^2(\alpha+\beta)}{4B\sqrt{A-B}},$$

$$C_3 = \frac{(2\alpha + \sqrt{2}\sqrt{A-B})(-\alpha^2+\beta^2+B) + 4J^2(\alpha-\beta) + 4K^2(\alpha+\beta)}{4B\sqrt{A-B}},$$

$$C_4 = \frac{(2\alpha + \sqrt{2}\sqrt{A+B})(\alpha^2-\beta^2+B) - 4J^2(\alpha-\beta) - 4K^2(\alpha+\beta)}{4B\sqrt{A+B}},$$

$$D_1 = \frac{iJ((\alpha-\beta)^2+B-4K^2)}{\sqrt{2}B\sqrt{A+B}}, \quad D_2 = \frac{iJ(-(\alpha-\beta)^2+B+4K^2)}{\sqrt{2}B\sqrt{A-B}},$$

$$D_3 = \frac{iK((\alpha+\beta)^2+B-4J^2)}{\sqrt{2}\sqrt{A+B}}, \quad D_4 = \frac{iK(-(\alpha+\beta)^2+B+4J^2)}{\sqrt{2}B\sqrt{A-B}}.$$

Meanwhile, the analytical expression of Eq. (2) under Configuration B are given by

$$\begin{aligned}
a_1(t) &= (C_1' - C_4')\sinh(\theta_1') + (C_2' + C_3')\sinh(\theta_2') - (C_1' + C_4')\cosh(\theta_1') + (C_3' + C_2')\cosh(\theta_2'),\\
a_2(t) &= D_1'\sinh(\theta_1') + D_2'\sinh(\theta_2'),\\
a_3(t) &= \frac{2JK}{B'}[\cosh(\theta_2') - \cosh(\theta_1')] - \frac{\sqrt{2}JK(\alpha+\beta)}{B'\sqrt{A+B'}}\sinh(\theta_1') + \frac{\sqrt{2}JK(\alpha+\beta)}{B'\sqrt{A-B'}}\sinh(\theta_2'),\\
a_4(t) &= \frac{iJ(\alpha-\beta)}{B'}[\cosh(\theta_1') - \cosh(\theta_2')] + D_3'\sinh(\theta_1') + D_4'\sinh(\theta_2').
\end{aligned}$$

Here $B' = \sqrt{(\alpha^2-\beta^2)^2 + 4J^2[4K^2 - (\alpha-\beta)^2]}$, $\theta_1' = \frac{t\sqrt{A+B'}}{\sqrt{2}}$, $\theta_2' = \frac{t\sqrt{A-B'}}{\sqrt{2}}$,

$$C_1' = \frac{(2\alpha - \sqrt{2}\sqrt{A+B'})(\alpha^2-\beta^2+B') + 4J^2(\beta-\alpha)}{4\sqrt{2}B'\sqrt{A+B'}}, \quad C_2' = \frac{(2\alpha - \sqrt{2}\sqrt{A-B'})(-\alpha^2+\beta^2+B') + 4J^2(\alpha-\beta)}{4\sqrt{2}B'\sqrt{A-B'}},$$

$$C_3' = \frac{(2\alpha + \sqrt{2}\sqrt{A-B'})(-\alpha^2+\beta^2+B') + 4J^2(\alpha-\beta)}{4\sqrt{2}B'\sqrt{A-B'}}, \quad C_4' = \frac{4J^2(\alpha-\beta) - (2\alpha + \sqrt{2}\sqrt{A+B'})(\alpha^2-\beta^2+B')}{4\sqrt{2}B'\sqrt{A+B'}},$$

$$D_1' = \frac{iK(\alpha^2-\beta^2+B'-4J^2)}{\sqrt{2}B'\sqrt{A+B'}}, \quad D_2' = \frac{iK(-\alpha^2+\beta^2+B'+4J^2)}{\sqrt{2}B'\sqrt{A-B'}}, \quad D_3' = \frac{iJ((\alpha-\beta)^2+B'-4K^2)}{\sqrt{2}B'\sqrt{A+B'}},$$

$$D_4' = \frac{iJ(-(\alpha-\beta)^2+B'+4K^2)}{\sqrt{2}B'\sqrt{A-B'}}.$$

[1] I. Rotter, J. Phys. A: Math. Theor. **42**, 153001 (2009).

[2] C. M. Bender, D. C. Brody, and H. F. Jones, Phys. Rev. Lett. **89**, 270401 (2002).

[3] C. M. Bender, Europhysics News **47**, 17 (2016).

[4] Z. H. Musslimani, K. G. Makris, R. El-Ganainy, and D. N. Christodoulides, Phys. Rev. Lett. **100**, 030402 (2008).

[5] F. Minganti, A. Miranowicz, R. W. Chhajlany, and F. Nori, Phys. Rev. A **100**, 062131 (2019).

[6] Ş. K. Özdemir, S. Rotter, F. Nori, and L. Yang, Nat. Mater. **18**, 783 (2019).

[7] A. Mostafazadeh, J. Math. Phys. **43**, 205 (2002).

[8] C. M. Bender and S. Boettcher, Phys. Rev. Lett. **80**, 5243 (1998).

[9] Z. Ahmed, Phys. Lett. A **282**, 343 (2001).

[10] V. V. Konotop, J. Yang, and D. A. Zezyulin, Rev. Mod. Phys. **88**, 035002 (2016).

[11] Z. Ahmed, Phys. Lett. A **290**, 19 (2001).

[12] A. Mostafazadeh, J. Math. Phys. **43**, 3944 (2002).

[13] Z. Lin, H. Ramezani, T. Eichelkraut, T. Kottos, H. Cao, and D. N. Christodoulides, Phys. Rev. Lett. **106**, 213901 (2011).

[14] B. Peng, Ş. Özdemir, S. Rotter, H. Yilmaz, M. Liertzer, F. Monifi, C. Bender, F. Nori, and L. Yang, Science **346**, 328 (2014).

[15] C. M. Bender, B. K. Berntson, D. Parker, and E. Samuel, Am. J. Phys. **81**, 173 (2013).

[16] Y.-L. Liu, R. Wu, J. Zhang, Ş. K. Özdemir, L. Yang, F. Nori, and Y.-x. Liu, Phys. Rev. A **95**, 013843 (2017).

[17] W. D. Heiss, J. Phys. A: Math. Theor. **45**, 444016 (2012).

[18] M. Parto, Y. G. Liu, B. Bahari, M. Khajavikhan, and D. N. Christodoulides, Nanophoton. **10**, 403 (2020).

[19] Z. Zhang, Z. Yang, and J. Hu, Phys. Rev. B **102**, 045412 (2020).

[20] W. Xiong, Z. Li, Y. Song, J. Chen, G.-Q. Zhang, and M. Wang, Phys. Rev. A **104**, 063508 (2021).

[21] W. Xiong, Z. Li, G.-Q. Zhang, M. Wang, H.-C. Li, X.-Q. Luo, and J. Chen, Phys. Rev. A **106**, 033518 (2022).

[22] G.-Q. Zhang, Y. Wang, and W. Xiong, Phys. Rev. B **107**, 064417 (2023).

[23] Y. D. Chong, L. Ge, and A. D. Stone, Phys. Rev. Lett. **106**, 093902 (2011).

[24] L. Ge, Y. D. Chong, S. Rotter, H. E. Türeci, and A. D. Stone, Phys. Rev. A **84**, 023820 (2011).

[25] M. Liertzer, L. Ge, A. Cerjan, A. D. Stone, H. E. Türeci, and S. Rotter, Phys. Rev. Lett. **108**, 173901 (2012).

[26] A. Guo, G. J. Salamo, D. Duchesne, R. Morandotti, M. Volatier-Ravat, V. Aimez, G. A. Siviloglou, and D. N. Christodoulides, Phys. Rev. Lett. **103**, 093902 (2009).

[27] P. Chen and Y. D. Chong, Phys. Rev. A **95**, 062113 (2017).
[28] L. Feng, R. El-Ganainy, and L. Ge, Nat. Photon. **11**, 752 (2017).
[29] R. El-Ganainy, K. G. Makris, M. Khajavikhan, Z. H. Musslimani, S. Rotter, and D. N. Christodoulides, Nat. Phys. **14**, 11 (2018).
[30] J. Jia, B. Zhu, F. Ye, H. Zhong, and H. Deng, Eur. Phys. J. D **74**, 117 (2020).
[31] C. Dembowski, H.-D. Gräf, H. L. Harney, A. Heine, W. D. Heiss, H. Rehfeld, and A. Richter, Phys. Rev. Lett. **86**, 787 (2001).
[32] G.-Q. Zhang and J. Q. You, Phys. Rev. B **99**, 054404 (2019).
[33] S.-B. Lee, J. Yang, S. Moon, S.-Y. Lee, J.-B. Shim, S. W. Kim, J.-H. Lee, and K. An, Phys. Rev. Lett. **103**, 134101 (2009).
[34] K. Takata and M. Notomi, Phys. Rev. Lett. **121**, 213902 (2018).
[35] W.-C. Wang, Y.-L. Zhou, H.-L. Zhang, J. Zhang, M.-C. Zhang, Y. Xie, C.-W. Wu, T. Chen, B.-Q. Ou, W. Wu, H. Jing, and P.-X. Chen, Phys. Rev. A **103**, L020201 (2021).
[36] L. Ding, K. Shi, Q. Zhang, D. Shen, X. Zhang, and W. Zhang, Phys. Rev. Lett. **126**, 083604 (2021).
[37] G.-Q. Zhang, Z. Chen, D. Xu, N. Shammah, M. Liao, T.-F. Li, L. Tong, S.-Y. Zhu, F. Nori, and J. Q. You, PRX Quantum **2**, 020307 (2021).
[38] W.-Y. Wang, B. Sun, and J. Liu, Phys. Rev. A **106**, 063708 (2022).
[39] J. Dong, X.-L. Li, F.-Q. Dou, and W.-Y. Wang, Phys. Rev. A **108**, 063506 (2023).
[40] K. Li and P. G. Kevrekidis, Phys. Rev. E **83**, 066608 (2011).
[41] M. Duanmu, K. Li, R. Horne, P. Kevrekidis, and N. Whitaker, Phil. Trans. R. Soc. A. **371**, 20120171 (2013).
[42] K. Li, P. G. Kevrekidis, D. J. Frantzeskakis, C. E. Rüter, and D. Kip, J. Phys. A: Math. Theor. **46**, 375304 (2013).
[43] V. V. Konotop, D. Pelinovsky, and D. A. Zezyulin, Europhys. Lett. **100**, 56006 (2012).
[44] S. K. Gupta and A. K. Sarma, J. Mod. Opt. **61**, 227 (2014).
[45] M. Kreibich, J. Main, H. Cartarius, and G. Wunner, Phys. Rev. A **87**, 051601(R) (2013).
[46] C. M. Bender and H. F. Jones, J. Phys. A: Math. Theor. **44**, 015301 (2011).
[47] A. Mostafazadeh, Int. J. Geom. Methods Mod. Phys. **07**, 1191 (2010).
[48] M. Kozlov and G. P. Tsironis, New J. Phys. **17**, 105004 (2015).
[49] G. S. Agarwal and K. Qu, Phys. Rev. A **85**, 031802(R) (2012).
[50] D. W. S. nleber, A. Eisfeld, and R. El-Ganainy, New J. Phys. **18**, 045014 (2016).
[51] J. Naikoo, K. Thapliyal, S. Banerjee, and A. Pathak, Phys. Rev. A **99**, 023820 (2019).
[52] X.-W. Xu, Y.-X. Liu, C.-P. Sun, and Y. Li, Phys. Rev. A **92**, 013852 (2015).
[53] Z. Zhang, Y. Zhang, J. Sheng, L. Yang, M.-A. Miri, D. N. Christodoulides, B. He, Y. Zhang, and M. Xiao, Phys. Rev. Lett. **117**, 123601 (2016).
[54] Y. Kagan, A. E. Muryshev, and G. V. Shlyapnikov, Phys. Rev. Lett. **81**, 933 (1998).
[55] M. Kreibich, J. Main, H. Cartarius, and G. Wunner, Phys. Rev. A **90**, 033630 (2014).
[56] C. Hang and G. Huang, Phys. Rev. A **98**, 043840 (2018).
[57] S. Longhi, Phys. Rev. B **80**, 235102 (2009).
[58] K. G. Makris, R. El-Ganainy, D. N. Christodoulides, and Z. H. Musslimani, Phys. Rev. Lett. **100**, 103904 (2008).
[59] S. Longhi, Phys. Rev. Lett. **103**, 123601 (2009).
[60] M. C. Zheng, D. N. Christodoulides, R. Fleischmann, and T. Kottos, Phys. Rev. A **82**, 010103(R) (2010).
[61] K. Zhang, W. Chen, M. Bhattacharya, and P. Meystre, Phys. Rev. A **81**, 013802 (2010).
[62] M. Greiner, O. Mandel, T. W. Hänsch, and I. Bloch, Nature (London) **419**, 51 (2002).
[63] S. Tung, V. Schweikhard, and E. A. Cornell, Phys. Rev. Lett. **97**, 240402 (2006).
[64] O. Morsch and M. Oberthaler, Rev. Mod. Phys. **78**, 179 (2006).
[65] A. Mostafazadeh, J. Math. Phys. **43**, 2814 (2002).
[66] C. M. Bender and P. D. Mannheim, Phys. Lett. A **374**, 1616 (2010).
[67] K. Li, P. G. Kevrekidis, B. A. Malomed, and U. G. nther, J. Phys. A: Math. Theor. **45**, 444021 (2012).
[68] C. A. Downing, D. Zueco, and L. Martin-Moreno, ACS Photon. **7**, 3401 (2020).
[69] A. C. Bleszynski-Jayich, W. E. Shanks, B. Peaudecerf, E. Ginossar, F. von Oppen, L. Glazman, and J. G. E. Harris, Science **326**, 272 (2009).
[70] C. Shu, K. Zhang, and K. Sun, Phys. Rev. B **109**, 184302 (2024).
[71] A. Melkani and J. Paulose, Phys. Rev. E **110**, 015003 (2024).